





Evaluating the performance of OCT in assessing static and potential dynamic properties of the retinal ganglion cells and nerve fiber bundles in the living mouse eye

PENGFEI ZHANG,^{1,2}  OLGA VAFAEVA,³ CHRISTIAN DOLF,³
YANHONG MA,¹ GUOZHEN WANG,¹ JESSICA CHO,² HENRY
HO-LUNG CHAN,^{4,5} NICHOLAS MARSH-ARMSTRONG,³ AND ROBERT
J. ZAWADZKI^{2,6,*} 

¹School of Optoelectronic Engineering and Instrumentation Science, Dalian University of Technology, Dalian, 116024, China

²UC Davis EyePod Small Animals Ocular Imaging Laboratory, University of California Davis, Davis, CA 95616, USA

³Department of Ophthalmology & Vision Science, University of California Davis Eye Center, 4860 Y Street, Suite 2400, Sacramento, CA 95817, USA

⁴Laboratory of Experimental Optometry (Neuroscience), School of Optometry, The Hong Kong Polytechnic University, Hong Kong, China

⁵Research Centre for SHARP Vision (RCSV), The Hong Kong Polytechnic University, Hong Kong, China

⁶Center for Human Ocular Imaging Research (CHOIR), Dept. of Ophthalmology & Vision Science, University of California Davis, 4860 Y Street, Suite 2400, Sacramento, CA 95817, USA

*rjzawadzki@ucdavis.edu

Abstract: Glaucoma is a group of eye diseases characterized by the thinning of the retinal nerve fiber layer (RNFL), which is primarily caused by the progressive death of retinal ganglion cells (RGCs). Precise monitoring of these changes at a cellular resolution in living eyes is significant for glaucoma research. In this study, we aimed to assess the effectiveness of temporal speckle averaging optical coherence tomography (TSA-OCT) and dynamic OCT (dOCT) in examining the static and potential dynamic properties of RGCs and RNFL in living mouse eyes. We evaluated parameters such as RNFL thickness and possible dynamics, as well as compared the ganglion cell layer (GCL) soma density obtained from *in vivo* OCT, fluorescence scanning laser ophthalmoscopy (SLO), and *ex vivo* histology.

© 2023 Optica Publishing Group under the terms of the [Optica Open Access Publishing Agreement](#)

1. Introduction

Glaucoma is the leading cause of irreversible blindness in the adult population worldwide [1]. The global prevalence of glaucoma was estimated to be 60 million in 2010 and 80 million in 2020, and it is on track to affect 112 million people worldwide by 2040 [2]. Glaucoma is a group of eye conditions that damage the optic nerve, as measured by thinning of the retinal nerve fiber layer (RNFL), the health of which is vital for good vision. This damage ultimately results in the degeneration and death of retinal ganglion cells (RGCs) [3] and visual field loss, although the order that the damage occurs may depend upon multiple factors [4]. Many forms of glaucoma have no warning signs. The deterioration is so gradual that one may not notice a change in vision until the condition is at an advanced stage. Vision loss caused by glaucoma cannot be recovered using available medical treatments. The best possible management of this disease is to slow down or prevent its progression [5]. Therefore, in addition to laboratory-based functional assessments that have been suggested for diagnosing and monitoring glaucoma [6,7], there is a growing need for the development of noninvasive *in vivo* imaging tools that can provide greater sensitivity and

specificity than current methods. Such tools would allow for the longitudinal and quantitative monitoring of subtle changes in cellular features affected by glaucoma.

Mouse models of glaucoma have contributed greatly to the understanding of glaucoma pathophysiology and the screening of potentially therapeutic drugs [8–10]. Traditional ways to evaluate therapies longitudinally often require sacrificing many mice and *ex vivo* retina imaging with microscopy to quantify the RGCs somas and RNFL loss [8]. Nowadays, due to the progress in genetic engineering, the RGCs and their axons can be fluorescently labeled in transgenic mouse lines, enabling single-cell imaging of RGCs (somas and axons) in the living mouse eye [11,12], as shown in the examples in Fig. 1, which shows several examples of *in vivo* imaging of the retinal ganglion cells in mice using extrinsic fluorescent proteins, thanks to the availability of transgenic mice lines and viral transfection with GFP reporter gene. Figure 1 (a) shows wide-field *in vivo* SLO fluorescence imaging of the retina in a transgenic mouse expressing Thy1-YFP-H, where yellow fluorescent protein (YFP) is specifically expressed in a subset of retinal ganglion cells (RGCs). While Fig. 1 (b) is a zoom-in view, providing detailed structures of the cell. In Fig. 1 (c) and (e), wide-field *in vivo* SLO fluorescence imaging displays the retinal fluorescence in a transgenic mouse expressing mCherry and GFP under the control of the Brn3b and Isl2 promoters, respectively. Both are markers for specific types of RGC. Figure 1 (d) and (f) are zoomed-in views, showcasing the mCherry- and GFP-labeled RGCs where individual cells can be well identified. In Fig. 1 (g), wide-field *in vivo* SLO fluorescence imaging captures the retinal fluorescence in a mouse transduced with an adeno-associated viral vector type 2 (AAV2) containing EGFP labeling the mitochondria. Figure 1 (h) offers a more detailed look at the EGFP-labeled structures in the retina, showing potential mitochondrial localization within RGCs. However, there is still an unmet need for imaging the health of the retina without fluorescent labels, using techniques that are directly comparable to the clinical settings. Developing and using the same techniques and biomarkers in pre-clinical studies and clinical trials are needed.

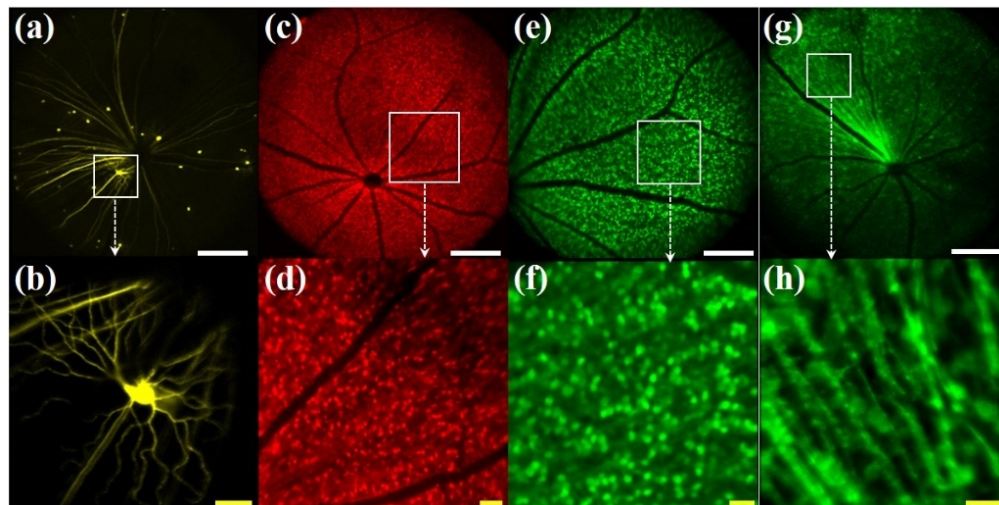


Fig. 1. Wide-field (top) and zoom-in (bottom) *in vivo* SLO fluorescence imaging of the retinas in four transgenic mice expressing fluorescence in different RGCs types imaged in our lab [13]: (a, b) B6.Thy1-YFP-H [14]; (c, d) Brn3b-mCherry [15]; (e, f) Isl2-GFP [16]; (g, h) AAV2:MitoEGFPmCHERRY [17]. Scale bars: 400 μ m (white), 50 μ m (yellow).

Optical coherence tomography (OCT) is a noninvasive imaging technology used to obtain high-resolution two- and three-dimensional (2D and 3D) images of semitransparent objects, such as the retina [18]. Retinal layers can be differentiated by OCT based on their varying

light scattering properties, which allows precise measurements of individual layer thicknesses [19–21]. However, standard OCT systems lack sufficient resolution and contrast to differentiate individual GCL somas in humans. Thus, clinical screenings for glaucoma focus on imaging and quantification of the optic nerve head (ONH) morphology and measuring the thickness of the RNFL. Although indirect, measuring macula GCL thinning is also feasible and may be a good way to assess RGC soma loss in a clinical setting [22,23]. Recently, a novel OCT variant utilizing adaptive optics to enhance OCT lateral resolution (AO-OCT) was developed. It greatly reduced speckle noise and increased the contrast of OCT images, which enabled clear visualization of the GCL somas in the human retina after averaging hundreds of precisely-aligned and series-acquired AO-OCT volumes [24]. We applied this concept to OCT/OCTA data in mouse retina imaging and developed a framework to register and analyze large number of serially acquired OCT volumes, and we named the procedure temporal speckle averaging OCT (TSA-OCT) [25]. Here we applied TSA-OCT to quantify the GCL soma count and compare the results with the RGC soma count in the transgenic mouse line expressing fluorescence proteins in RGCs using fluorescence scanning laser ophthalmoscopy (fSLO).

One limitation of TSA-OCT is that it can only extract static structural information of the retina due to the low sampling volume rate (~ 0.1 Hz). Recently, researchers developing full-field OCT (FF-OCT) demonstrated that metabolically driven dynamic scattering changes of cellular structures could be used to generate additional contrast in FF-OCT imaging [26–29]. Therefore, we decided to apply a similar framework to our regular B-scan-based scanning OCT [30], referred to as dynamic OCT (dOCT). We implemented dOCT acquisition and processing to obtain the dynamic information of the RNFL and potential RGCs.

To demonstrate the accuracy and alignment of these techniques for imaging RGC and the RNFL, in this paper we first imaged a mouse eye longitudinally for a week and the thicknesses of the RNFL at different locations and time points were extracted and compared to demonstrate the measurement accuracy of TSA-OCT. Second, the mouse eye was imaged with dOCT and the dynamic scattering properties of the retinal tissue were evaluated using temporal Fourier Analysis of the serially acquired OCT Data. Third, the eye of a mouse with GFP-labeled RGCs was imaged using fSLO and TSA-OCT, and the numbers of GCL somas visualized by both modalities were counted and compared. Finally, the TSA-OCT was validated with *ex vivo* microscopy imaging of the same retinas flat-mounted and immuno-stained with RGC molecular markers.

2. Methods

2.1. *In vivo* Imaging system and protocol

Our lab has developed a dedicated custom-built instrument for *in vivo* mouse retina imaging. It combines two optical imaging modalities, fSLO and OCT [31], and is referred to later in the text as a combined SLO/OCT system. fSLO can perform fluorescence imaging with excitation wavelengths of 488/561 nm and emission wavelengths centered at 525/609 nm with corresponding bandwidths of 45/54 nm, respectively. The system is capable of imaging both GFP- and mCherry-labeled cells simultaneously. It has a 50-degree field of view and can zoom up to 50 times. The scanning speed can be adjusted through software, with a pixel dwell time ranging from 10 to 2 microseconds, corresponding to a point scan speed of 100kHz to 500kHz. The fluorescence signals are directed to the PMTs via a multi-mode fiber with a 4 airy disk aperture. The lateral resolution at the retina was measured to be $2.9\ \mu\text{m}$ [14], and the corresponding estimated axial resolution is $\sim 100\ \mu\text{m}$. OCT uses a broadband OCT light source (M-T-850-HP-I, Superlum) with an experimentally validated axial resolution of $3.6\ \mu\text{m}$ and an estimated lateral resolution of $5\ \mu\text{m}$. The OCT can run in volumetric or B-scan data acquisition mode (Fig. 2) to perform either TSA-OCT or dOCT techniques as described below.

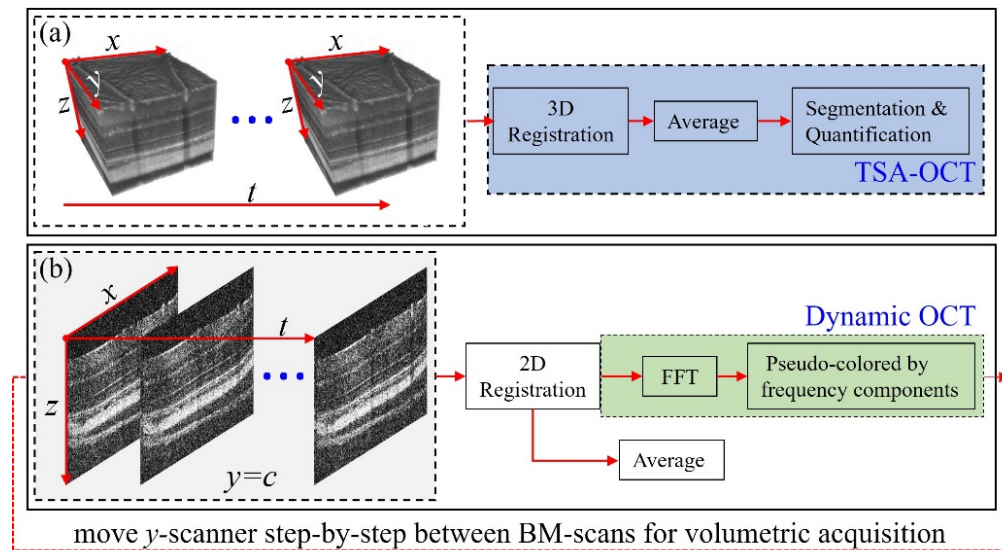


Fig. 2. The imaging protocols for TSA-OCT and dynamic OCT, (a) repeated volumes were acquired and registered in 3D, then averaged to get images with enhanced quality, finally, the data were segmented and quantified, (b) repeated B-scans (BM-scan) were acquired for each dynamic OCT session to probe higher frequency components, after 2D registration, FFT along the temporal direction was performed to extract different frequency components of the retina dynamics; to cover the region-of-interest(ROI), y-scanner needs to be moved step-by-step after each BM-scan.

2.2. Temporal speckle averaging OCT (TSA-OCT):

The OCT system can be configured to run in TSA-OCT mode, as shown in Fig. 2 (a). Briefly, the system acquires serially multiple OCT volumes ($512 \times 512 \times 2048$ pixels) from the same retinal region ($\sim 600 \times 600 \mu\text{m}^2$) at a 100 kHz A-scan rate to collect 20-100 volumes depending on the experimental design. Due to the eye motion caused by breathing, head movement, and small eye movements, consequent motion artifacts occur during retinal imaging. Thus, the core of TSA-OCT processing requires precise 3D registration between serially-acquired volumes. In our previous work, we developed a framework that was appropriate for mouse retinal imaging, and the technical detail could be found in [25]. Further averaging of co-registered volumes greatly increases the cellular contrast in the OCT images, allowing clear visualization of the RNFL (formed by RGC axons) and enabling visualization of the individual GCL somas.

2.3. Dynamic OCT (dOCT)

Single 3D data cube acquisition for TSA-OCT takes about 2.6 s / volume, corresponding to 0.4 Hz (volume acquisition rate), which is too slow to probe the dynamic changes of the retina. Hence, the OCT was re-configured to run at repeated BM-scan mode (as shown in Fig. 2 (b)) with a B-scan acquisition rate of 25 Hz while the A-scan acquisition rate remained at 100 kHz. During each in-plane imaging, 100 B-scans were acquired, which takes 4 seconds. The B-scans were co-registered with ImageJ 'MultiStackReg' plugin applying rigid body translation, and FFT was performed on each pixel along the temporal direction to extract the frequency information [30]. Note that, the frequency analysis of dOCT was performed on logarithmic amplitude OCT.

The temporal variation of each (x, z) location in the BM-Scan was assessed using Fast Fourier Transform (FFT). When considering a BM-Scan with N B-scans and a sampling frequency of f_s , the frequency bin number is calculated as $N/2 + 1$. The interval (or bin size) between two

adjacent frequency bins is determined as $f_{\text{step}} = f_s/N$. Then, the resulting frequency spectrum components were categorized into three distinct bands:

1. The static component, corresponding to the 1st frequency bin (0 Hz).
2. Low-frequency dynamic components, encompassing the 2nd to the $0.1 \times N$ frequency bins ($f_s/N - 0.1 f_s$).
3. High-frequency dynamic components, spanning from the $0.1 \times N + 1$ to $N/2$ frequency bins ($(0.1 f_s + 1) - f_s/2$).

Then the frequency components were divided into three parts: static component (band (1)), middle (band(2)), and high band (band(3)). Each color channel was normalized from 0-1 (and remapped to 16-bit for display purpose). For display, the image contrast of three-color channels was enhanced using contrast-limited adaptive histogram equalization. Finally, a 3×3 median filter was applied to green and red channels. They were further used as red, green, and blue channels of an RGB image to form a pseudo-color image, encoding dynamic information of the tissue. These processing steps were developed primarily by following two previous dOCT publications [30,32]. Note that the non-linear process of the contrast-limited adaptive histogram equalization makes it less straight-forward to understand the distributions. To map the volumetric tissue dynamics, the y-scanner position needs to be moved in between two adjacent BM-scan sessions to probe consecutive planes in the retinal volume. In the current configuration, acquiring dOCT data sets takes about 8.5 minutes for 128 y-scans spanned over the volume.

2.4. Extraction of circumpapillary B-scans from TSA-OCT volumes

In human clinical imaging, the circumpapillary retinal nerve fiber layer thickness (cRNFLt) is an important metric for diagnosing glaucoma [33]. And it is also of great interest in mouse research, and, with averaging, both near-infrared and visible light OCT [34] can give enhanced contrast of the nerve fiber bundles. Human RNFL is relatively thick (~ 20 - $100 \mu\text{m}$) and hence, its thickness can be measured accurately by standard OCT. However, the mouse RNFL thickness ($\sim < 10 \mu\text{m}$ [35]) is close to the axial resolution of OCT, and hence it is hard to be accurately assessed by standard OCT. TSA-OCT can improve the image quality [25] and hence can enhance the accuracy of RNFL thickness measurement of mice.

Figure 3 demonstrated a wide-field TSA-OCT for a B6-albino mouse to visualize the RNFL layer for testing the performance of the method. In total, 50 OCT volumes over a wide field-of-view (FOV, 50°) were collected and processed to obtain TSA-OCT volumetric data set. The *enface* retinal layers containing RNFL for single and averaged volumes were segmented and shown in Fig. 3 (a) and (c), respectively, in which the nerve fiber bundles were much clearer in the TSA-OCT data. The virtual circumpapillary B-scans (cB-scans) were also extracted for comparison from single and TSA-OCT volumes and shown in Fig. 3 (b) and (d), respectively, in which the image quality of RNFL was also dramatically increased by the TSA method. Note that, a breathing motion artifact can be observed just superior to the ONH in Fig. 3(c), which is coming from the mouse breath captured by the reference volume, thus, preserved in the volume-averaged TSA image.

When comparing RNFL images across different measurements, a co-registration was necessary requiring the correction of the position of individual cB-scans at different days in relation to the cB-scan at the initial imaging session (day0). To achieve this, we applied the following sequential procedure:

1. Initially, we conducted a global search to the position of the maximum of cross-correlation within the central region ($\pm 2^\circ$ or $\pm 72 \mu\text{m}$) by using a grid of 21×21 points evenly distributed over the search area.

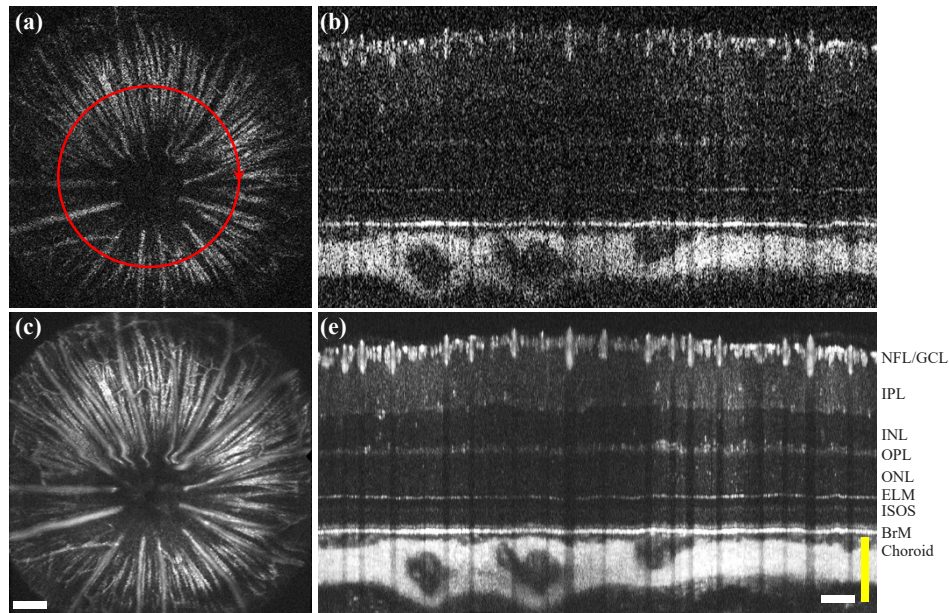


Fig. 3. Visualizations of TSA-OCT volume acquired in a B6-albino mouse: (a, c) *enface* RNFL C-scan intensity images for single and TSA-OCT volumes, respectively; (b, d) The virtual circumferential B-scans (position shown by the red circle in (a)) flattened to their BrM layers for single and TSA-OCT volumes, respectively. Scale bar: 200 μm (white) / 100 μm (yellow). Abbreviations: NFL/GCL – nerve fiber layer/ganglion cell layer; IPL/OPL – inner/outer plexiform layer; INL/ONL – inner/outer nuclear layer; ELM – external limiting membrane; IS/OS – inner/outer segment junction; BrM – Bruch’s membrane. Mouse genotype: B6-albino.

- Subsequently, a fine search was performed to the position of the maximum of cross-correlation with a 21×21 grid centered around the maximum point found in the global search, with a smaller range ($\pm 0.1^\circ$ or $\pm 3.6 \mu\text{m}$).
- To determine the optimal rotation angle of the cB-scans relative to their initial positions, a similar searching process was applied with 51 steps, spanning $\pm 6^\circ$.

Thus, this procedure was repeated 933 times in total, for co-registration of each consecutive cB-scan to the reference one. The thickness of RNFL in each image was calculated by manually selecting 30 pairs of points at the upper and lower edges of the RNFL. The positions of the blood vessels were excluded from thickness measurements.

2.5. *Ex vivo microscopy evaluation of flat-mounted retina*

To achieve co-registration of *ex vivo* and *in vivo* data, vasculature in flat-mounted retinas, where the ventral retina was marked by a deep incision, was labeled with IB4-lectin conjugated to Alexa-647 and RGCs were labeled with rabbit anti-Rbpms detected with either donkey anti-rabbit Cy3 or anti-rabbit Alexa 488 secondary. Whole retinas were then imaged with $10\times$ magnification ($\text{NA} = 0.25$), at 11 μm z-steps to capture all vascular plexuses, and 10% overlap between tiles, using a Zeiss Apotome-2 microscope. To facilitate initial co-registration of *ex vivo* and *in vivo* images, the vessel features in both images were visually identified and matched. The *ex vivo* image was cropped to match the image size of the *in vivo* result. This process enabled comparison and analysis of the corresponding features in both *ex vivo* and *in vivo* images.

For immunohistochemistry, mice were euthanized, and the eyes enucleated and immersion fixed for 1-2 hours in 4% paraformaldehyde (PFA). Retinas were dissected out and flat-mounted after several incisions, followed by an additional overnight 4% PFA immersion fixation weighed down under a coverslip, also at 4°C. After blocking with 5% normal donkey serum in phosphate-buffered saline (PBS) with 0.03% Triton X-100 overnight at 4°C, retinas were incubated for 3 additional nights in the same solution containing anti-Rbpms primary antibody (GTX118619, Genetex), diluted 1:700. After three 1 hour washes in the same solution without antibodies, retinas were incubated overnight in filtered 1:250 dilutions of either donkey anti-rabbit Cy3 or anti-rabbit Alexa 488 secondary antibody (111-165-144, Jackson ImmunoResearch; A11034, Invitrogen), also in the same solution, followed by three washes in PBS, an overnight incubation in a 1:1000 dilution of Isolectin GS-IB4, AlexaFluor 647 (132450, Invitrogen) in PBS and additional three washes in PBS, all before mounting under a coverslip in Aqua-Polymount media (18606-20, Polysciences).

2.6. Mouse models and animal handling

1. Transgenic mouse lines with GFP fluorescently labeled RGCs.

The mouse transgenic line expressing GFP in most RGCs, Tg(Isl2-GFP)LW124Gsat/Mmucd, was obtained from the Mutant Mouse Regional Resource Center (MMRRC) and is a re-combineered Bacterial Artificial Chromosome transgene generated by the GENSAT BAC Transgenic Project [15], its expression in RGCs has been characterized by others [16].

2. Animal handling.

All mouse husbandry and handling protocols were approved by the University of California's Institutional Animal Care and Use Committee, which strictly adheres to all guidelines of the NIH and satisfies those of the Association for Research in Vision and Ophthalmology (ARVO) for animal use. Adult Isl2-GFP, B6 (C57BL/6J), and B6-albinos (B6(Cg)-Tyr^c-2J/J) mice were used. B6 refers to the C57BL/6 mouse strain, which is a widely used inbred strain of laboratory mice in biomedical research. The use of B6 mice in research is rationalized by their well-defined genetic background, consistent physiology, and reproducible behavior, which make them useful for studying a variety of diseases and conditions. Alternatively, B6-albinos are a sub-strain of B6 mice that are commonly used in vision research due to their lack of melanin pigment, which makes it possible to visualize the Bruch's membrane and separate the apical side of retinal pigment epithelium (RPE) and rod outer segment tips (ROST) [36]. In our study, B6 mice were used as the wild type of ISL2-GFP mice.

Mice were typically 2 months old at the time of imaging, obtained either from our collaborators or from the Jackson Laboratory, and maintained on a 12:12 hr, ~100-lux light cycle. During measurements, they were anesthetized with inhalational isoflurane (2% to 2.5% in O₂), and their pupils were dilated with medical-grade tropicamide (1%) and phenylephrine (2.5%). A contact lens and gel (GelTeal Tears, Alcon, USA) were used to maintain good tear film quality and corneal transparency during *in vivo* retinal imaging.

3. Study protocol.

Here, we collected the data with TSA-OCT and compared the results to images of the RGCs in the transgenic mouse line expressing GFP in RGCs. Please note that our study specifically focuses on examining the Ganglion Cell Layer (GCL) and Retinal Nerve Fiber Layer (RNFL) using dOCT and TSA-OCT. The reason for this particular focus is directly related to the primary objective of our study in the long term, which is to investigate the possible effects of glaucoma on the retina. GCL and RNFL are two known structures to

be affected by glaucoma, hence our choice to concentrate on these specific areas in our research.

3. Results

3.1. *In vivo* TSA-OCT imaging of the nerve fiber bundles

We longitudinally imaged an Isl2-GFP mouse for a week on days 0, 2, 4, and 7 with TSA-OCT, in which 20 serial OCT volumes were acquired over the same 50° FOV and processed. The results of image processing of these data are shown in Fig. 4. The cB-scans with 5 different radii (r), (7.5°, 10°, 12.5°, 15°, 17.5° FOV corresponding to 255 μm , 340 μm , 425 μm , 510 μm , and 595 μm on retina respectively) as shown in Fig. 4 (a), were extracted to check the RNFL thickness at different locations. The resulting cB-scans were cropped to cover the RNFL only and are shown in Fig. 4 (b), showing a decreasing trend of the RNFL thickness from the inner to the outer circles. The cB-scans corresponding to the green circles ($r = 10^\circ$ or 340 μm) acquired on different days and displayed using enhanced contrast (using saturation 0.1% of the pixels) were shown in Fig. 4 (c), showcasing good repeatability of the measurements.

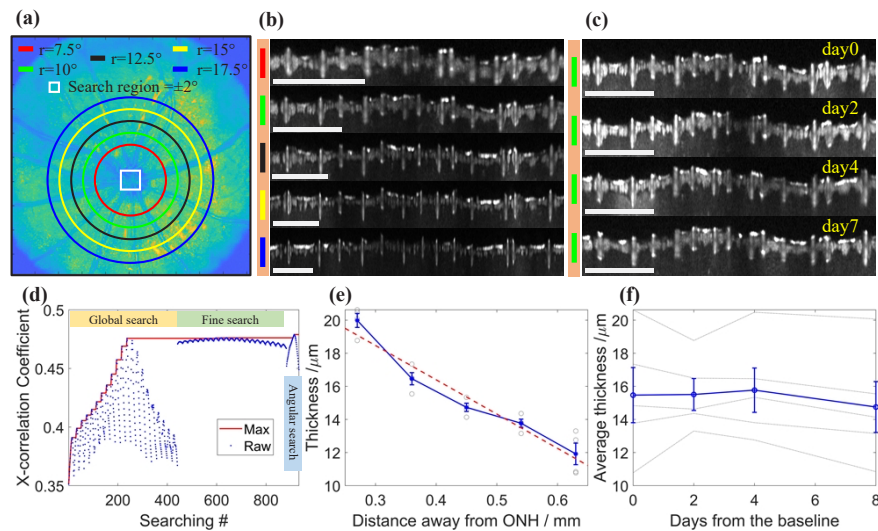


Fig. 4. Quantification of the nerve fiber layer thickness. (a) sketch of the circumpapillary B-scans with different radii; (b) the cropped B-scans showing the nerve fiber layers, the color bars match the color of the circles in (a); (c) the cropped B-scans showing the nerve fiber layers for the green circles at different days; (d) the searching process in matching circumpapillary B-scans at different days, with the searching region indicating by the white square in (a); (e) the RNFL thickness changes along the distance away from ONH; (f) the average RNFL thickness at different days, the five faint lines were the individual measurements along the five different circles in panel (a). Scale bars: 500 μm . Errorbar: ± 1 S.E.M. Mouse genotype: Isl2-GFP.

The cross-correlation coefficient between the reference cB-scan acquired at day 0 and the new cB-scan for consecutive days was calculated to give feedback to the searching algorithm. The resulting cross-correlation coefficients in a search process are shown in Fig. 4 (d). Then the average RNFL thicknesses of the cB-scans grouped by the different radii, (average distance from the ONH) were extracted and plotted, as shown in Fig. 4 (e). The averaged RNFL thickness was gradually decreasing with a nearly linear relationship in respect to the distance from ONH. To

test the repeatability of the RNFL measurements across different days, the data were reorganized and shown to the time (different days).

There is a variation of the thickness between different days in the order of a few μm . After further averaging the measurement results for five different diameter circles, the accuracy of the thickness measurement could be within μm (blue line in Fig. 4(f)), falling into the range of 15-16 μm after averaging of 5 different locations for each day.

3.2. *In vivo* dOCT imaging of the dynamic scattering properties of GCL and RNFL

The above TSA-OCT results provide static structure information, however, there is also dynamic information about the living tissue encoded in time-varying scattering from these structures. To access this information, we have modified our data acquisition protocol, as demonstrated in Fig. 5 (a-e), where 1000 BM-scans were acquired at the same location on the retina. This change was required to access relatively high-speed variations in scattering. After registration, the direct averaged gray scale image was shown in Fig. 5 (a) with 8 manually selected areas. Figure 5 (b) plots the time variance of these 8 images.

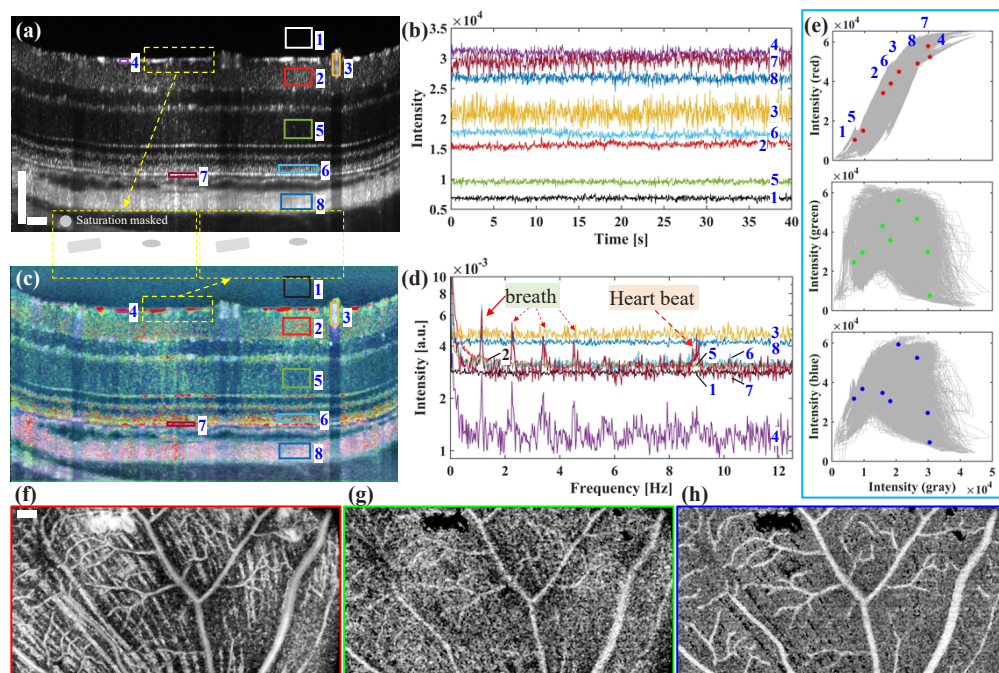


Fig. 5. Temporal analysis of OCT offers dynamic dOCT information about time-varying retinal scattering: (a) gray scale B-scan averaged from a 1000 series B-scans acquired at 25fps, (b) time series intensity variations of 8 representative areas indicating in panel (a), (c) pseudo-colored dOCT B-scan, (d) spectrum analysis of the 8 areas, with RGB colors from three frequency bands (marked by corresponding color on the frequency axis), (e) the pixel-to-pixel mapping between panel (a) and (c) for three colors, with the 8 areas marked by dots, (f-h) visualization of *enface* C-scans from RNFL/GCL by three separate frequency bands (f: static, g: medium motility, h: fast motility). Scale bars: 100 μm . Mouse genotype: B6-albino.

Each pixel was then color-coded in RGB to generate the color-coded dynamic OCT image (Fig. 5(c)), representing different frequency components contributing to the dOCT signal, where red represents the static component— or no motility, green represents medium motility, and blue represents fast motility. The spectrum analysis results from these 8 areas were shown in Fig. 5(d),

where the three frequency bands were marked by different color bars, respectively. Note that the spikes on the frequency curves are caused by mouse breathing with a fundamental frequency of ~ 1 Hz [37–39]. Limited by the sampling frequency (25 Hz), the fundamental frequency of ~ 9 Hz might be caused by the heart beat [39] and is shown on the frequency curve. Such retinal motion patterns caused by cardiorespiratory processes have already been reported [37–39]. Different colors indicate that the *in vivo* tissue dynamic properties vary across different retinal structures. A zoom-in comparison in the inner retina (yellow dashed rectangle in Fig. 5 (a, c)) is shown in between these two panels. The green spots showcase increased contrast in potential GCL soma structures, due to medium motility components, if compared with the average gray scale image. Note that a slightly different version of Fig. 5 (b) and (d) was provided in Supplement 1 Fig. S1 which may facilitate the comparison of the time-frequency spectra for the different layers.

The pixel-to-pixel mapping between the gray scale and the color-coded images were plotted in Fig. 5 (e), with the 8 representative areas marked by the corresponding dots. The red color intensity is generally linearly proportional to the gray scale intensity, which means bright structures in the gray scale image have stronger red components in the colored image. However, it is different for the other two channels. The strongest green and blue components appear roughly around half of the intensity of the gray scale image, which means the most dynamic parts of the tissue only have medium back-reflection properties. Finally, to obtain the volumetric dOCT data, a $512 (x) \times 50 (t) \times 256 (y) \times 2048 (z)$ dataset was acquired by rotating the Y-scanner to produce 256 laterally displaced BM-scan locations, with 50 frames in each BM-scan to be analyzed by dOCT, and 512 A-scan in each B-scan. The intensities of three frequency components from the *enface* C-scan corresponding to RNFL/Ganglion Cells Layer (GCL) are shown in Fig. 5 (f-h). The nerve fiber bundles and blood vessels were visualized in the static component (Fig. 5 (f)); however, most blood vessels can be identified in the intermediate frequency component (Fig. 5(g)); the high-frequency component (Fig. 5 (h)) offers the dynamic scattering information from retinal vasculature (similar to OCTA processing).

3.3. *In vivo validation of TSA-OCT with SLO images of fluorescence-labeled RGCs*

To identify whether the cell somas visualized in the retinal GCL by TSA-OCT corresponds to RGCs or not, a transgenic mouse (Isl2-GFP) with GFP labeled RGCs was imaged (Fig. 6) using combined SLO/OCT system. Both TSA-OCT and SLO (back-reflection and GFP fluorescence) data were acquired simultaneously. In total, 100 OCT volumes and 400 dual SLO/fSLO frames were collected and processed to produce TSA-OCT volume, SLO and fSLO images respectively.

The median averaged back-reflectance SLO image in Fig. 6 (a) provides the vascular map, which is used to fine-co-register the SLO image with the OCT image. Figure 6 (b) shows the median fSLO image in which the individual fluorescently-labeled RGCs can be visualized, with the yellow dots, shown in Fig. 6 (f), indicating the manually annotated 272 RGCs. When the variance instead of the median average is used for serial fSLO frames, the individual RGCs are easier to visualize and include weakly fluorescent cells (Fig. 6 (c)). The yellow 'x's, shown in Fig. 6 (f), are used to annotate the RGCs that were not visible in the median-averaged fSLO but become visible in the variance processing of serial fSLO frames, resulting in 52 more cells or $\sim 19\%$ increase in cell count (total of 324 cells). We think that the higher cell count is closer to the total number of fluorescently labeled RGC in this mouse. In Fig. 6 (c), it can be observed that the fluorescently labelled RGCs are more distinguishable in the variance fSLO data. We hypothesize that this increased visibility is a result of residual motion errors that occur during the registration of fSLO image series, leading to higher variance near the cell boundary and relatively lower variance within the cells. Consequently, this creates an illusion of larger cell size and higher contrast at the cell boundary.

Figure 6 (d) shows an *enface* single C-Scan slice extracted from TSA-OCT volume at GCL position revealing individual scattering spots which are hypothesized to represent individual

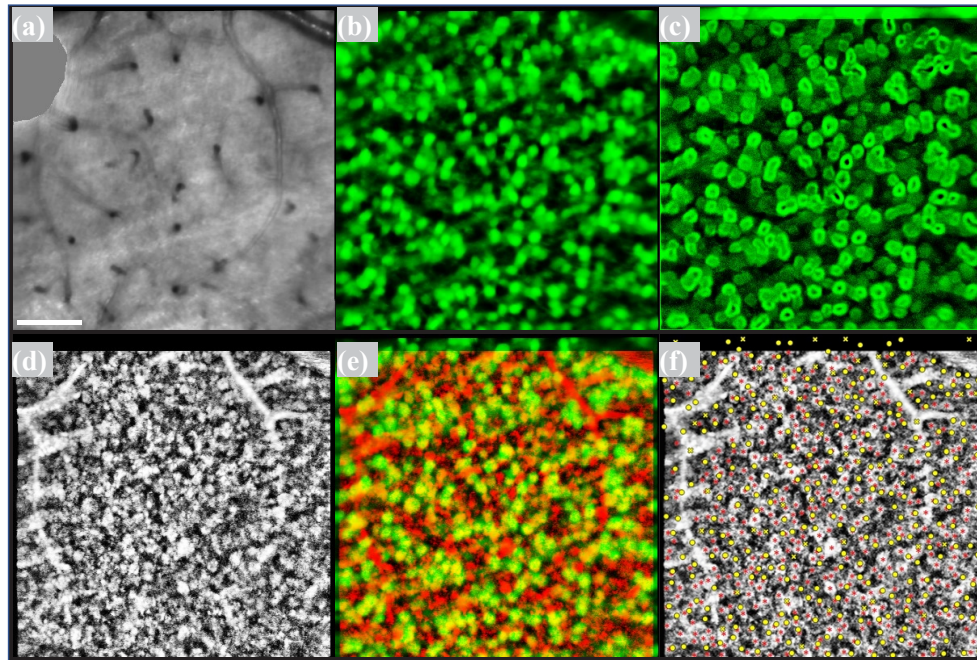


Fig. 6. Comparison of GCL somas visualizations and annotations using fSLO and TSA-OCT. (a) averaged SLO back-reflection image, note that RGC somas are not visible due to the low contrast, and only retinal capillaries (gray lines, capillaries laying in plane, and black spots, capillaries diving between retinal layers) can be seen, (b) median fSLO image (RGCs somas manually annotated by yellow dots), (c) STD variance of fSLO image (additional RGCs somas, not visible on median fSLO, annotated by yellow 'x's), (d) TSA-OCT *enface* layer extracted from GCL showing cell somas (annotated with red stars), (e) visualization of co-registered images from panel (b) (green color) and (d) (red color), (f) overlap between (d) and the RGC annotations from (c). Scale bar: 100 μm . Mouse genotype: Isl2-GFP.

GCL somas. The red stars, shown in Fig. 6 (f), were used to manually annotate 473 scattering spots corresponding to cell somas. We further co-displayed the median-averaged fSLO image with the TSA-OCT image by co-registering Fig. 6 (b) (in green) with Fig. 6 (d) (in red), resulting in a pseudo-color image where yellow spots indicate the cells visible in both fSLO and TSA-OCT. There are many red-colored spots left, which means that only a portion of the GCL somas annotated using OCT is fluorescently labeled as found on fSLO frames. This result is not surprising since only approximately 40% of all RGCs express Islet2 (Isl2), the LIM-homeodomain transcription factor used as a target in the creation of this transgenic mouse line [16].

Next, we overlapped the fSLO annotations onto the TSA-OCT image (Fig. 6 (f)) and excluded annotations that did not fall into the areas where OCT somas were visualized. It can be seen that the cell patterns do not well overlap with each other. As the data is acquired simultaneously and the capillaries are well-aligned, both imaging modalities are co-registered. The discrepancy may be attributed to distinct structures detected by the fSLO and TSA-OCT signals. Specifically, while fSLO primarily detects fluorescently labeled RGC somas, TSA-OCT could capture not only the RGC cell's somas but also the somas of other cell types. We further conducted a detailed analysis of the numbers of GCL somas appearing in 'both OCT and fSLO', 'OCT only', and 'fSLO only' by applying a threshold to the distance between the soma centers identified in fSLO and OCT images. When the distance was shorter than the threshold, we categorized the two somas as appearing in 'both OCT and fSLO'. Otherwise, they were categorized as either 'OCT

only' or 'fSLO only'. With a threshold set to 10 μm , the counts were 183 for 'both OCT and fSLO', 290 for 'OCT only', and 141 for 'fSLO only'. However, with a threshold of 5 μm , the counts changed to 38 for 'both OCT and fSLO', 435 for 'OCT only', and 286 for 'fSLO only'. Nonetheless, further exploration is necessary to ascertain the relatively low correlation between structures seen on TSA-OCT and fSLO. Moreover, higher-resolution *in vivo* imaging could facilitate better co-localization of the cells.

Finally, the ratio of the number of cells annotated using fSLO to the number of cells annotated using TSA-OCT images was calculated to be 55.6% (for median fSLO) and 65.5% (for variance fSLO), respectively (with 9 and 14 subtracted from 272 and 324 as the cell number from Fig. 6 (b) and (c), respectively). When using the median fSLO images as a "gold standard", this suggests that the number of RGCs visualized by TSA-OCT was about 80% higher than expected. This observation could be further validated by imaging and counting RGCs *ex vivo* in individual mice previously imaged *in vivo*.

3.4. Automatic annotation of fluorescently labeled GCL somas on fSLO and TSA-OCT images

We next implemented a machine-learning-based method for automatically counting the cells using the Trainable Weka Segmentation plugin in Fiji ImageJ [40]. The area of cells and background can be automatically segmented and separated, as shown in Fig. 7 (a-c), which were the segmented results for median fSLO (Fig. 6 (b)), variance fSLO (Fig. 6 (c)) and TSA-OCT (Fig. 6 (d)), respectively. For these images, the number of cells was counted to be 317, 287, and 514, respectively. And the average size of the cells was calculated to be 212, 350, and 150 pixels. It is noted that variance fSLO had the largest cell size because there was a built-in error of increasing cell size due to eye motion.

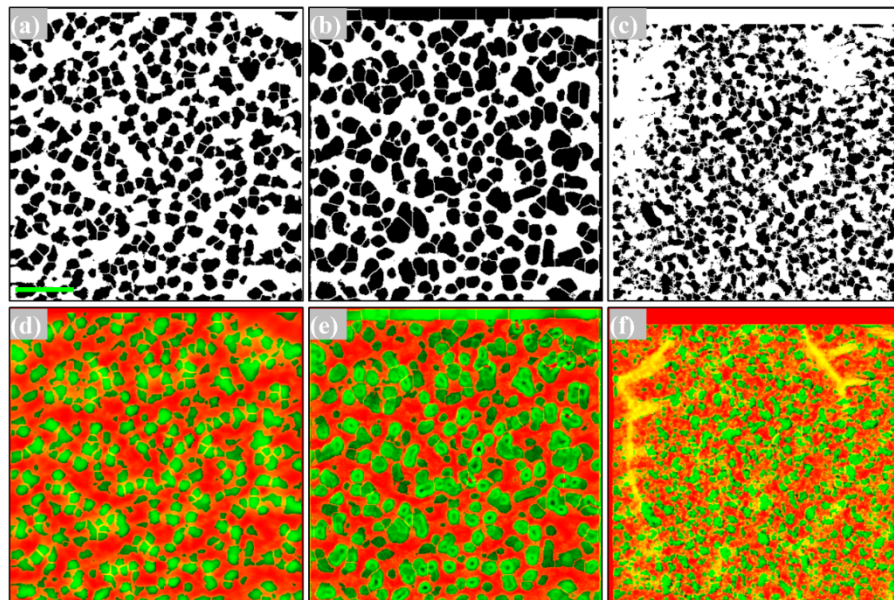


Fig. 7. Machine-learning-based automatic cell segmentation and annotation, (a-c) segmented cell masks from median fSLO, variance fSLO, and TSA-OCT, respectively, (d-f) projection of the masks (colored into red) onto the raw images (colored into green). Scale bar: 100 μm . Mouse genotype: Isl2-GFP.

To test the performance of the segmentation, the background of Fig. 7 (a-c) was filled with red, then the corresponding raw images were colored green. The merged images are shown in Fig. 7 (d-f). Because the brightness of the cells was much higher than the background in the fSLO images, Fig. 7 (d) and (e) showed good segmentation results. For the segmentation results in the TSA-OCT image, because the blood vessels have similar brightness to the scattering cells, they appeared as yellow color in merging with the red background (Fig. 7 (f)). Overall, these numbers are close to that of manual annotations, with errors of 16.5%, -11.4%, and 8.7%, respectively. Nevertheless, the average numbers of cells annotated using these two types of analysis were 295, 305, and 494, respectively. Considering the corresponding areas were 0.25 mm², 0.25 mm², and 0.236 mm², the resulting RGC densities in these images were 1180, 1220, and 2093 cells/mm², for median fSLO, variance fSLO, and TSA-OCT respectively.

3.5. Correlation of *in vivo* and *ex vivo* images for validation of *in vivo* results

To validate the *in vivo* RGC visualization results, *ex vivo* images of the same retina were performed for comparison. A mouse retina was first imaged with wide FOV TSA-OCT/OCTA to generate the *enface* images (as shown in Fig. 8 (a) and (b), respectively). Then, two zoom-in regions were imaged with TSA-OCT to get the fine structures of the retina (Fig. 8 (c) and (d)). Then, the animal was sacrificed, the retina was flat-mounted and immunostained with molecular markers for the retinal vasculature. The vascular map of a flat-mounted retina imaged by a commercial microscope is shown in Fig. 8 (e), in which two zoom-in OCT imaging locations corresponding to Fig. 8 (c) and (d) are marked by yellow and purple rectangles. The vascular patterns can be roughly matched between *in vivo* and *ex vivo* data although with considerable distortion. Nevertheless, this further confirms that a co-registration between *in vivo* and *ex vivo* results down to the vascular level is feasible [41–43].

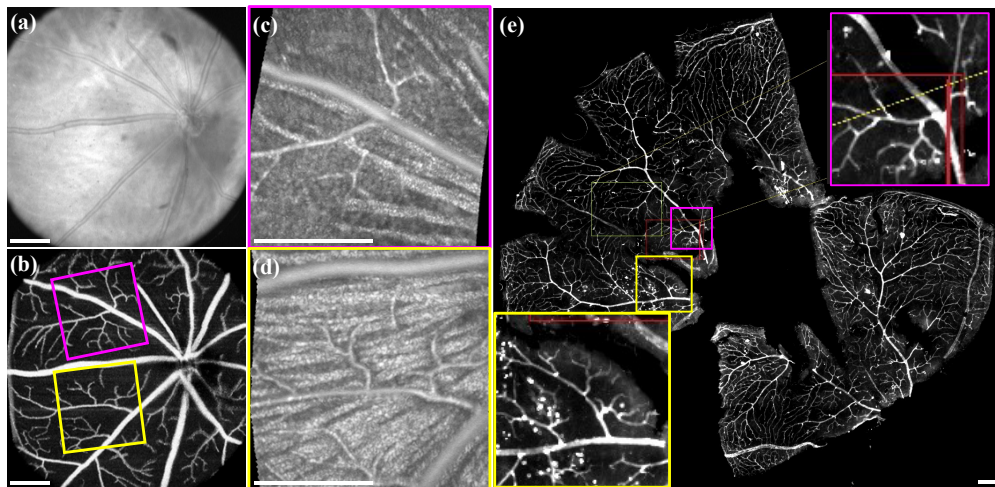


Fig. 8. Co-registration of the *in vivo* TSA-OCT data with the *ex vivo* flat-mounted histology of the same retina using the vascular map. (a, b) the large FOV TSA-OCT and TSA-OCTA *enface* projections, respectively, (c, d) two zoom-in TSA-OCT *enface* C-Scans from RNFL/GCL showcasing the two locations where the vascular maps matching that in panel (b), (e) the vascular patterns corresponding to panel (c), and (d) can be identified on the flat-mount histology. Scale bar: 300 μm. Mouse genotype: B6.

To test the correlation between *in vivo* and *ex vivo* RGC imaging, another mouse was imaged first by a wide field OCTA to get the vascular map (Fig. 9 (a) medium inset), followed by a 3× zoom-in TSA-OCT imaging (Fig. 9 (a) small inset) with a few key vessels co-registered between

OCTA and TSA-OCT indicated by the yellow arrows. The reason why the TSA-OCT image in Fig. 9 (a) need to be zoomed in is to limit the total number of pixels in each volume, which is necessary to achieve a feasible volume acquisition speed. In our case, the number of A-scans per B-scan was limited to 512 to satisfy the requirement of the sampling theorem, which restricts the field of view. Despite the smaller field of view, the TSA-OCT provides fine information about the retina with high resolution and sensitivity.

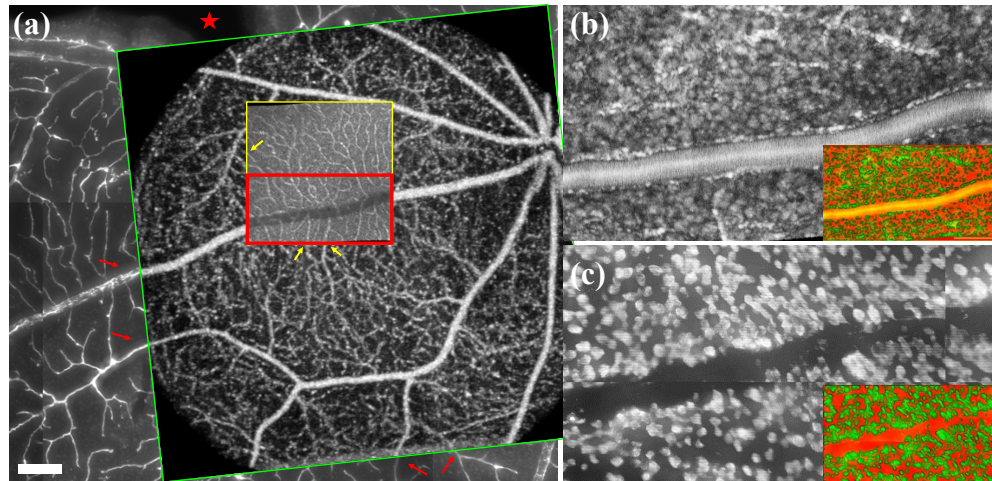


Fig. 9. Visualization of co-registration between *in vivo* TSA-OCT results and the flat-mounted histology using the vascular map as fiduciary reference. (a) the cropped flat-mounted image of the retina with immunochemical fluorescence staining of the vasculature with the corresponding wide-FOV OCTA *enface* (medium inset) and the zoom-in TSA-OCT *enface* (small inset), shows the good co-registration between the vessels (red and yellow arrows), (b, c) side-by-side comparison between GCL somas visualized by *in vivo* TSA-OCT (b) and *ex vivo* RGCs immunochemically stained with anti-Rbpms (c). The zoom-in image location is indicated by the red rectangle in panel (a). The corresponding automatic segmentation results were shown by the colored insets in (b) and (c). Scale bar: 200 μm . Mouse genotype: B6.

Next, the animal was sacrificed and the retina flat-mounted and immunostained with molecular markers for retinal vasculature and GFP expressing RGC. The cropped image of the flat-mounted vasculature map is shown in Fig. 9 (a), where several key vessels are matching each other between *in vivo* OCTA and the *ex vivo* flat-mounted image, indicated by the red arrows. Note that the overlay of the OCTA image doesn't perfectly match the flat-mounted results, especially the shadows of the vessels crossing the top of the insert cannot be observed. This is because the retina was distorted during the flat-mounted process. E.g., there is a tear indicated by the red arrow in Fig. 9 (a). Figure 9 (b) and (c) show examples of co-registration between the GCL somas seen on *in vivo* (TSA-OCT) and *ex vivo* (microscope) images, where the location site was marked by the red rectangle in Fig. 9 (a).

It should be noted that there is a noticeable difference between the TSA-OCT images in Fig. 9 (a) and (b). For instance, the large vessel appears blacked out in Fig. 9 (a) while it appears bright in Fig. 9 (b). The reason for this is that the image plane in Fig. 9 (a) was selected to be around OPL to capture fine vessel structures and match the large field OCTA image, while the image plane in Fig. 9 (b) was selected to be around GCL to maximize the appearance of the GCL somas. As the large vessel is located closer to GCL and far away from OPL, it appears black in Fig. 9 (a) and bright in Fig. 9 (b).

Given the distortion during the retinal flat-mount process, it is hard to correlate the images down to the cellular levels. However, a comparison between the total annotated cells and their densities is feasible. The counting of the annotated cells for Fig. 9 (b) and (c) are 1129 and 534, respectively, and are shown in Fig. 9 (b) and (c) insets. As seen in Fig. 9 (b) the number RGC somas is over-estimated given that some of the nerve fibers were annotated as a series of cells, while the *ex vivo* image of cells annotation shown in Fig. 9 (c) is more reliable. Given that the imaging area is 0.222 mm^2 , the corresponding RGC cell densities in these images are 5085 and 2405 cells/ mm^2 .

4. Discussion and conclusion

Glaucoma is a leading cause of irreversible blindness worldwide. RGC dysfunction and death are the fundamental pathogenesis by which glaucoma causes irreversible vision loss [3]. Thus, *in vivo* assessment of the RGC structure and function can provide deep insight into the pathophysiology of glaucoma and facilitate the development of novel treatment strategies. However, *in vivo* detection of RGC loss in the human eye has been challenging. It is only recently possible to image these neurons using high-speed and high-resolution OCT through sophisticated processes [24,44], and pilot study was done to demonstrated soma loss detection [45]. As an important and beneficial supplement to clinical research, preclinical research with animal models possesses more freedom and wider scope in identifying new biomarkers, and testing new treatments. These advanced imaging technologies have the potential to assess the structure and function of RGCs in animal models, thus sensitively monitor the cells' status alternation under aging, disease, and treatments, which could provide insightful information on clinical glaucoma research.

4.1. Cell density variations in different imaging modalities and sessions

We compared the counting results in Fig. 9 to the literature, with an average number of ~ 3000 cells/ mm^2 [46] ranging between 2000 to 8000 cells/ mm^2 from the dorsal retina to the temporal optic disk [47]. In the mid-peripheral zone, where we usually perform our imaging, the RGC density is ~ 3200 cells/ mm^2 with a total cell density within the GCL of ~ 8000 cells/ mm^2 [48,49] including displaced amacrine cells (DAC), vascular endothelial cells (VEC), and nuclei with non-distinct features (ND) [49]. This indicates that the cells seen by OCT could include all these cells while the flat-mounted image should visualize the RGCs only.

In contrast, the cells densities in Fig. 6 and 7 were ~ 1200 and ~ 2100 cells/ mm^2 for *in vivo* fluorescence labeling and TSA-OCT counting, which is significantly lower than the density measured in Fig. 9 (~ 2400 and ~ 5000 cells/ mm^2 by fluorescence and TSA-OCT, respectively). The difference between *in vivo* and *ex vivo* fluorescence (1200 vs. 2400), could be due to the RGC labeling efficiency of *in vivo* method which is $\sim 40\%$ of the total RGCs, while the *ex vivo* method labels almost 100% of the total RGCs. However, the two TSA-OCT counting results vary a lot (2100 vs. 5000). Although the clear reason for this discrepancy is unknown, it could be due to the spatial variation of the cell distribution [47] or the ability to image individual RGC somas in different animals during independent imaging sessions.

The mouse strain used for Fig. 6 and Fig. 7 was the Isl2-GFP mouse, whereas the B6 mouse stained with anti-Rbpms was used for Fig. 8 and Fig. 9. Each experiment was conducted once, and the presented results primarily aim to report the specific protocols of data acquisition and processing, including the framework of *ex vivo* validation. However, it is important to note that repeated measurements and statistical analysis with a larger number of animals are necessary to further explore and discuss any potential differences in cell counts between these two measurements. Therefore, these preliminary results should be interpreted with caution and considered as a starting point for future investigations.

The OCT resolution and contrast in our current system are limited, making it difficult to identify GCL somas in the mouse retina. However, we observe bright spots corresponding to

GCL somas, similar to human imaging [24]. In contrast, Grieve et al. demonstrated a different appearance of GCL somas in rodents using full-field OCT (FF-OCT), where they appear as black rather than bright spots observed in humans, primates, pigs, and sheep [50]. As discussed in their publication, this contrast inversion can arise from two factors: 1) differences in the proportion of displacement amacrine cells (dAC) within the GCL among species, and 2) differences in the nuclear morphology of RGCs and dAC [50]. In addition to the difference of the imaging techniques (point scan OCT vs. FF-OCT), we speculate that the major reason for the appearance difference between our results and theirs is that our TSA-OCT results were obtained from living mouse eyes, while their results were obtained from *ex vivo* flat-mounted retina.

4.2. Difficulties in registering and comparing the *in vivo* and *ex vivo* images

Registration and comparison of *in vivo* and *ex vivo* images at cellular level for retina imaging is a challenging task due to several factors. First, these images were acquired under different imaging modalities and instruments. The *in vivo* results were acquired under fSLO and TSA-OCT, while the *ex vivo* results were acquired under a traditional confocal fluorescence microscopy. Second, distortion is a major factor. Although the averaging technique removed most of the motion artifacts in the *in vivo* imaging, there is still distortion introduced by the alignment. The distortion is particularly heavy for the *ex vivo* retina during the complex sample preparation process for flat mounted microscopy imaging. Additionally, the imaging field of view and image quality can also vary significantly between the two modalities. Moreover, the inherent differences in the properties of the tissue can be a challenge. *In vivo* imaging is performed on live tissue, which can exhibit different optical properties than fixed *ex vivo* tissue. This can result in differences in the intensity and contrast of the images obtained from the two modalities. Furthermore, the process of fixing the tissue can cause changes in the tissue structure and composition, which can further complicate the comparison of *in vivo* and *ex vivo* images.

4.3. Further investigations are necessary to fully understand the potential of TSA-OCT in advancing glaucoma research

As shown in this work, TSA-OCT can quantify some of the structural information about GCL somas and their axons in mouse models, which could develop novel biomarkers for early detection and sensitive monitoring progression of glaucoma. However, it is still in a preliminary stage which demonstrates the capability of the technique, there is much unknown about the physiological and pathological structural changes under different conditions. For example, optic nerve crush (ONC) is common, acute and with rapid retinal structural [51] changes, although it might not be ideal to mimic glaucoma in general, it is a more efficient way to study physiological changes of the RGCs and soma during their deaths. In addition, high intra-ocular pressure (IOP) is a well-known risk factor of glaucoma, there are multiple ways to elevate the IOP to induce glaucomatous damages in the animal eyes, such as acute ocular hypertension [52] or chronic ocular hypertension [53]. What's more, there are a plethora of genetic models of glaucoma in mice that provide valuable resources for studying the disease, including the DBA/2J mouse, Myocilin mutant mouse, and Optineurin, Cyp11b1, and Tbk1 knockout mice [54]. The diversity of animal model makes it a powerful way to study the alternations of cellular structure during the progression of glaucoma, further investigations with various animal models are necessary to fully understand the potential of TSA-OCT in advancing glaucoma research.

4.4. Notes to the dOCT results

Please note that in the current data acquisition process of dOCT in Fig. 2 (b), the lateral motion of the sample can contribute to the dOCT signal. While the lateral motion may be on the order of 10 μm over an 800-second period for anesthetized mice [25], it's important to emphasize that this motion can occur in both *x*-, *y*-, and *z*-directions. The existing 2D registration method effectively

corrects for x - and z -motions to a certain extent; however, it does not address y -direction (out of B-scan plane) motion. To address this limitation, one could develop imaging system with 3D tracking capabilities and real-time motion compensation, which holds the potential to mitigate this issue.

The breathing motion and the heartbeat are prominent signals in the frequency domain, but their impact on dOCT signals could not be identified in the image (Fig. 5 (c)). This discrepancy may be attributed to two factors. Firstly, the process of averaging between frequency bands tends to attenuate the amplitude of these signals, rendering them less pronounced. Secondly, the impact of breathing motion and the heartbeat extends beyond localized effects and manifests as a background, rather than producing conspicuous, isolated bright features in the image.

As shown in Fig. 5 (e) and described in paragraph 3 of section 3.2, the intensity of the color channels also depends on the SNR of the signals (monotonic dependence for $I(\text{red})$; increasing, then decreasing for $I(\text{green})$ and $I(\text{blue})$). As the retinal layers have intrinsically different reflectivity, one source of the observed color differences is the SNR.

The green spots are well observed in the x - z image in Fig. 5(c) inset but it is surprising that the potential GCL somas do not show up in the x - y projection of $I(\text{green})$ in Fig. 5(g). There are two possible reasons for the observed differences between Fig. 5 (c) and Fig. 5 (g): Firstly, the number of B-scans used to generate the dOCT image varies, with 1000 B-scans for Fig. 5 (c) and 50 for Fig. 5 (g). Secondly, the sampling density, measured by the A-scan number in each B-scan, differs, with 1024 for Fig. 5 (c) and 512 for Fig. 5 (g). These variations are due to the longtime of volumetric dOCT data acquisition. For instance, if Fig. 5 (g) were to follow Fig. 5 (c), it would take 2772 seconds (~46 minutes) to acquire a full-volume of dOCT dataset. We acknowledge that a more rigorous comparison should be conducted in the future with improved data acquisition speed and post-processing speed. Additionally, parallel detection schemes including Line Field OCT and Full Field OCT could allow more efficient detection of dOCT signal.

In Fig. 5 (h), surprisingly, the dark strips oriented along the RNFL bundles indicates there is less high-frequency signal at the bundles, although there is known dynamic mitochondrial transport within the RGC axons [55,56].

While the exact source of the dynamic information remains unknown, we hypothesize that it could be attributed to the movement of organelles within the cellular structures. However, the cellular mechanisms underlying this phenomenon have yet to be elucidated. To gain a deeper understanding, further analysis involving the integration of dOCT with super-resolution fluorescence microscopy may offer valuable insights. Nonetheless, it's worth noting that conducting such studies within the living eye presents substantial challenges.

4.5. Other functional OCT methods studying GCL soma dynamics

As a similar way to dOCT, the temporal correlation method developed by Kurokawa et al. [45] based on adaptive optics OCT could capture the temporal dynamics of GCL somas and revealed significant differences in time constant between individual GCL somas. In contrast, optoretinogram (ORG) is a newly developed technique [44,57–65] at the nascent stage to objectively assess neuronal function at the single cell level. To date, only a couple of groups in the world have demonstrated ORG to evaluate cone photoreceptor function. However, although evidence may exist [66,67], there have been no convincing cellular-level objective assessment methods of the RGC function in the living eye. When comparing these three methods, dOCT and temporal correlation AO-OCT can be used to enhance the visibility or classification of GCL somas, while ORG-based GCL soma function measurement, if successful, can precisely quantify GCL soma activities in response to visible light stimulus. Nevertheless, the ability to reliably image the structure of GCL somas and quantitatively assess their function using these methods would represent a significant milestone in ophthalmology research.

4.6. Final remarks

In conclusion, here we used a custom-made mouse retinal SLO/OCT system for serial volumetric imaging and applied the TSA-OCT and dynamic OCT techniques to visualize and annotate the RGCs somas and retinal nerve fiber bundles in vivo. Multi-modal imaging combining fluorescence and scattered light detection facilitates the comparison of the visibility of RGC somas seen by TSA-OCT with the gold standard of fluorescently labeled RGCs. TSA-OCT also greatly improves the quality of nerve fiber imaging, enabling precise measurement of the RNFL thickness for different retinal locations and over time. Additionally, dOCT processing revealed the changes in the temporal variation of OCT signal in the RNFL. This observation should be further validated by decoupling dOCT signal from SNR and gross tissue movements. Nevertheless, it has the potential to probe motility within the RNFL, a potentially useful biomarker of RGC health. The images of the cell structures have been further validated by correlating our in vivo results with ex vivo images acquired on the same retinas. As a preliminary study, this demonstrates the potential of TSA-OCT and dOCT to aid in the quantification of the glaucoma-related structural changes in the living mouse eye, which may help to investigate some key questions in basic science glaucoma research.

Funding. BrightFocus Foundation (G2021017S); National Science Foundation (IUCRC CBSS Grant); National Eye Institute (P30 EY012576, R01 EY026556); National Natural Science Foundation of China (62175024); Dalian University of Technology (DUT21RC(3)001, DUT21YG121).

Acknowledgments. We would like to acknowledge the generous contribution of Prof. Edward N. Pugh, Jr, and the support of Dr. Suman Manna and Dr. Sarah J. Karlen from UCD EyePod. We would like to thank our collaborator Prof. Anna La Torre from UC Davis.

Disclosures. The authors declare no conflicts of interest.

Data availability. Data underlying the results presented in this paper are not publicly available at this time but may be obtained from the authors upon reasonable request.

Supplemental document. See [Supplement 1](#) for supporting content.

References

1. J. B. Jonas, T. Aung, R. R. Bourne, *et al.*, "Glaucoma," *Lancet* **390**(10108), 2183–2193 (2017).
2. Y. C. Tham, X. Li, T. Y. Wong, *et al.*, "Global prevalence of glaucoma and projections of glaucoma burden through 2040: a systematic review and meta-analysis," *Ophthalmology* **121**(11), 2081–2090 (2014).
3. M. H. Kuehn, J. H. Fingert, and Y. H. Kwon, "Retinal ganglion cell death in glaucoma: mechanisms and neuroprotective strategies," *Ophthalmol Clin North Am* **18**(3), 383–395, (2005).
4. D. C. Hood, "Does retinal ganglion cell loss precede visual field loss in glaucoma?" *J Glaucoma* **28**(11), 945–951 (2019).
5. K. S. Yadav, R. Rajpurohit, and S. Sharma, "Glaucoma: Current treatment and impact of advanced drug delivery systems," *Life Sci.* **221**, 362–376 (2019).
6. P. H. Chu, H. H. Chan, and B. Brown, "Glaucoma detection is facilitated by luminance modulation of the global flash multifocal electroretinogram," *Invest. Ophthalmol. Vis. Sci.* **47**(3), 929–937 (2006).
7. H. H. Chan, Y. F. Ng, and P. H. Chu, "Applications of the multifocal electroretinogram in the detection of glaucoma," *Clin Exp Optom* **94**(3), 247–258 (2011).
8. B. P. Buckingham, D. M. Inman, W. Lambert, *et al.*, "Progressive ganglion cell degeneration precedes neuronal loss in a mouse model of glaucoma," *J. Neurosci.* **28**(11), 2735–2744 (2008).
9. I. Soto, E. Oglesby, B. P. Buckingham, *et al.*, "Retinal ganglion cells downregulate gene expression and lose their Axons within the optic nerve head in a mouse glaucoma model," *J. Neurosci.* **28**(2), 548–561 (2008).
10. S. J. McKinnon, C. L. Schlamp, and R. W. Nickells, "Mouse models of retinal ganglion cell death and glaucoma," *Exp. Eye Res.* **88**(4), 816–824 (2009).
11. C. K. S. Leung, R. N. Weinreb, Z. W. Li, *et al.*, "Long-term in vivo imaging and measurement of dendritic shrinkage of retinal ganglion cells," *Invest. Ophthalmol. Visual Sci.* **52**(3), 1539–1547 (2011).
12. Y. Geng, A. Dubra, L. Yin, *et al.*, "Adaptive optics retinal imaging in the living mouse eye," *Biomed. Opt. Express* **3**(4), 715–734 (2012).
13. J. Goetz, Z. F. Jessen, A. Jacobi, *et al.*, "Unified classification of mouse retinal ganglion cells using function, morphology, and gene expression," *Cell Rep.* **40**(2), 111040 (2022).
14. P. Zhang, M. Goswami, A. Zam, *et al.*, "Effect of scanning beam size on the lateral resolution of mouse retinal imaging with SLO," *Opt. Lett.* **40**(24), 5830–5833 (2015).

15. E. F. Schmidt, L. Kus, S. Gong, *et al.*, "BAC transgenic mice and the GENSAT database of engineered mouse strains," *Cold Spring Harbor Protocols* **2013**(3), pdb.top073692 (2011).
16. J. W. Triplett, W. Wei, C. Gonzalez, *et al.*, "Dendritic and axonal targeting patterns of a genetically-specified class of retinal ganglion cells that participate in image-forming circuits," *Neural development* **9**(1), 2 (2014).
17. C.-h. O. Davis, K.-Y. Kim, E. A. Bushong, *et al.*, "Transcellular degradation of axonal mitochondria," *Proc. Natl. Acad. Sci.* **111**(26), 9633–9638 (2014).
18. D. Huang, E. A. Swanson, C. P. Lin, *et al.*, "Optical coherence tomography," *Science* **254**(5035), 1178–1181 (1991).
19. F. A. Medeiros, L. M. Zangwill, C. Bowd, *et al.*, "Evaluation of retinal nerve fiber layer, optic nerve head, and macular thickness measurements for glaucoma detection using optical coherence tomography," *Am. J. Ophthalmol.* **139**(1), 44–55 (2005).
20. O. Tan, V. Chopra, A. T. H. Lu, *et al.*, "Detection of macular ganglion cell loss in glaucoma by fourier-domain optical coherence tomography," *Ophthalmology* **116**(12), 2305–2314.e2 (2009).
21. J. C. Mwanza, J. D. Oakley, D. L. Budenz, *et al.*, "Macular ganglion cell-inner plexiform layer: automated detection and thickness reproducibility with spectral domain-optical coherence tomography in glaucoma," *Invest. Ophthalmol. Visual Sci.* **52**(11), 8323–8329 (2011).
22. M. Santorini, T. F. De Moura, S. Barraud, *et al.*, "Comparative evaluation of Two SD-OCT macular parameters (GCC, GCL) and RNFL in chiasmal compression," *Eye Brain* **14**(5), 35–48 (2022).
23. A. Ahmed, A. A. Jammal, T. Estrela, *et al.*, "Intraocular pressure and rates of macular thinning in glaucoma," *Ophthalmology Glaucoma* **6**(5), 457–465 (2023).
24. Z. Liu, K. Kurokawa, F. Zhang, *et al.*, "Imaging and quantifying ganglion cells and other transparent neurons in the living human retina," *Proc. Natl. Acad. Sci.* **114**(48), 12803–12808 (2017).
25. P. Zhang, E. Miller, S. Manna, *et al.*, "Temporal speckle-averaging of optical coherence tomography volumes for in-vivo cellular resolution neuronal and vascular retinal imaging," *Neurophotonics* **6**(04), 1 (2019).
26. C.-E. Leroux, F. Bertillot, O. Thouvenin, *et al.*, "Intracellular dynamics measurements with full field optical coherence tomography suggest hindering effect of actomyosin contractility on organelle transport," *Biomed. Opt. Express* **7**(11), 4501–4513 (2016).
27. C. Apelian, F. Harms, O. Thouvenin, *et al.*, "Dynamic full field optical coherence tomography: subcellular metabolic contrast revealed in tissues by interferometric signals temporal analysis," *Biomed. Opt. Express* **7**(4), 1511–1524 (2016).
28. O. Thouvenin, C. Boccara, M. Fink, *et al.*, "Cell motility as contrast agent in retinal explant imaging with full-field optical coherence tomography," *Invest. Ophthalmol. Visual Sci.* **58**(11), 4605–4615 (2017).
29. J. Scholler, V. Mazlin, O. Thouvenin, *et al.*, "Probing dynamic processes in the eye at multiple spatial and temporal scales with multimodal full field OCT," *Biomed. Opt. Express* **10**(2), 731–746 (2019).
30. M. Münter, M. v. Endt, M. Pieper, *et al.*, "Dynamic contrast in scanning microscopic OCT," *Opt. Lett.* **45**(17), 4766–4769 (2020).
31. P. Zhang, A. Zam, Y. Jian, *et al.*, "In vivo wide-field multispectral scanning laser ophthalmoscopy–optical coherence tomography mouse retinal imager: longitudinal imaging of ganglion cells, microglia, and Müller glia, and mapping of the mouse retinal and choroidal vasculature," *J. Biomed. Opt.* **20**(12), 126005 (2015).
32. T. Kohlfäerber, M. Pieper, M. Münter, *et al.*, "Dynamic microscopic optical coherence tomography to visualize the morphological and functional micro-anatomy of the airways," *Biomed. Opt. Express* **13**(6), 3211–3223 (2022).
33. E. J. Lee, K. M. Lee, H. Kim, *et al.*, "Glaucoma diagnostic ability of the new circumpapillary retinal nerve fiber layer thickness analysis based on Bruch's membrane opening," *Invest. Ophthalmol. Visual Sci.* **57**(10), 4194–4204 (2016).
34. D. A. Miller, M. Grannonico, M. Liu, *et al.*, "Visible-light optical coherence tomography fibergraphy for quantitative imaging of retinal ganglion cell axon bundles," *Translational Vision Science & Technology* **9**(11), 11 (2020).
35. L. R. Ferguson, J. M. Dominguez Ii, S. Balaiya, *et al.*, "Retinal thickness normative data in wild-type mice using customized miniature SD-OCT," *PLOS ONE* **8**(6), e67265 (2013).
36. P. Zhang, B. Shibata, G. Peinado, *et al.*, "measurement of diurnal variation in rod outer segment length in vivo in mice with the oct optoretinogram," *Invest Ophthalmol Vis Sci* **61**(3), 9 (2020).
37. L. An, J. Chao, M. Johnstone, *et al.*, "Noninvasive imaging of pulsatile movements of the optic nerve head in normal human subjects using phase-sensitive spectral domain optical coherence tomography," *Opt Lett* **38**(9), 1512–1514 (2013).
38. E. O. H. Keith, S. Tilman, V. Clemens, *et al.*, "Measuring pulse-induced natural relative motions within human ocular tissue in vivo using phase-sensitive optical coherence tomography," *J. Biomed. Opt.* **18**(12), 121506 (2013).
39. B. Baumann, C. W. Merkle, M. Augustin, *et al.*, "Pulsatile tissue deformation dynamics of the murine retina and choroid mapped by 4D optical coherence tomography," *Biomed. Opt. Express* **13**(2), 647–661 (2022).
40. J. Schindelin, I. Arganda-Carreras, E. Frise, *et al.*, "Fiji: an open-source platform for biological-image analysis," *Nat Methods* **9**(7), 676–682 (2012).
41. S. Nakao, R. Arita, T. Nakama, *et al.*, "Wide-field laser ophthalmoscopy for mice: a novel evaluation system for retinal/choroidal angiogenesis in mice," *Invest. Ophthalmol. Visual Sci.* **54**(8), 5288–5293 (2013).
42. S. McLaren, A. L. Magno, D. Ramos, *et al.*, "Angiography reveals novel features of the retinal vasculature in healthy and diabetic mice," *Exp. Eye Res.* **138**, 6–21 (2015).

43. A. Ripolles-Garcia, G. Ruthel, G.-S. Ying, *et al.*, “Characterization of the canine retinal vasculature with optical coherence tomography angiography: comparisons with histology and fluorescein angiography,” *Front. Neuroanat.* **15**, 785249 (2021).
44. Z. Liu, F. Zhang, K. Zucca, *et al.*, “Ultrahigh-speed multimodal adaptive optics system for microscopic structural and functional imaging of the human retina,” *Biomed. Opt. Express* **13**(11), 5860–5878 (2022).
45. K. Kurokawa, J. Crowell A, F. Zhang, *et al.*, “Suite of methods for assessing inner retinal temporal dynamics across spatial and temporal scales in the living human eye,” *Neurophotonics* **7**(01), 1 (2020).
46. M. Salinas-Navarro, M. Jiménez-López, F. J. Valiente-Soriano, *et al.*, “Retinal ganglion cell population in adult albino and pigmented mice: A computerized analysis of the entire population and its spatial distribution,” *Vision Res.* **49**(6), 637–647 (2009).
47. U. C. Dräger and J. F. Olsen, “Ganglion cell distribution in the retina of the mouse,” *Invest. Ophthalmol. Visual Sci.* **20**, 285–293 (1981).
48. C.-J. Jeon, E. Strettoi, and R. H. Masland, “The major cell populations of the mouse retina,” *The Journal of Neuroscience* **18**(21), 8936–8946 (1998).
49. A. Hedberg-Buenz, M. A. Christopher, C. J. Lewis, *et al.*, “Quantitative measurement of retinal ganglion cell populations via histology-based random forest classification,” *Exp Eye Res* **146**, 370–385 (2016).
50. K. Grieve, O. Thouvenin, A. Sengupta, *et al.*, “Appearance of the retina with full-field optical coherence tomography,” *Invest. Ophthalmol. Visual Sci.* **57**(9), OCT96–OCT104 (2016).
51. S. Daniel, A. F. Clark, and C. M. McDowell, “Subtype-specific response of retinal ganglion cells to optic nerve crush,” *Cell Death Discovery* **4**(1), 67 (2018).
52. Y. Lakshmanan, F. S. Wong, W. Y. Yu, *et al.*, “Lycium barbarum polysaccharides rescue neurodegeneration in an acute ocular hypertension rat model under pre- and posttreatment conditions,” *Invest Ophthalmol Vis Sci* **60**(6), 2023–2033 (2019).
53. Y. Lakshmanan, F. S. Y. Wong, B. Zuo, *et al.*, “Longitudinal outcomes of circumlimbal suture model-induced chronic ocular hypertension in Sprague-Dawley albino rats,” *Graefes Arch Clin Exp Ophthalmol* **258**(12), 2715–2728 (2020).
54. I. H. Pang and A. F. Clark, “Inducible rodent models of glaucoma,” *Prog Retin Eye Res* **75**, 100799 (2020).
55. D.-Y. Yu, S. J. Cringle, C. Balaratnasingam, *et al.*, “Retinal ganglion cells: Energetics, compartmentation, axonal transport, cytoskeletons and vulnerability,” *Prog. Retinal Eye Res.* **36**, 217–246 (2013).
56. Y. A. Ito and A. Di Polo, “Mitochondrial dynamics, transport, and quality control: A bottleneck for retinal ganglion cell viability in optic neuropathies,” *Mitochondrion* **36**, 186–192 (2017).
57. D. Hillmann, H. Spahr, C. Pfäffe, *et al.*, “In vivo optical imaging of physiological responses to photostimulation in human photoreceptors,” *Proc Natl Acad Sci U S A* **113**(46), 13138–13143 (2016).
58. P. Zhang, R. J. Zawadzki, M. Goswami, *et al.*, “In vivo optophysiology reveals that G-protein activation triggers osmotic swelling and increased light scattering of rod photoreceptors,” *Proc Natl Acad Sci U S A* **114**(14), E2937–E2946 (2017).
59. V. P. Pandiyan, A. Maloney-Bertelli, J. A. Kuchenbecker, *et al.*, “The optoretinogram reveals the primary steps of phototransduction in the living human eye,” *Sci Adv* **6**(37), eabc1124 (2020).
60. M. Azimipour, D. Valente, K. V. Vienola, *et al.*, “Optoretinogram: optical measurement of human cone and rod photoreceptor responses to light,” *Opt Lett* **45**(17), 4658–4661 (2020).
61. A. Roorda, “Optoretinography is coming of age,” *Proc. Natl. Acad. Sci.* **118**(51), e2119737118 (2021).
62. A. Lassoued, F. Zhang, K. Kurokawa, *et al.*, “Cone photoreceptor dysfunction in retinitis pigmentosa revealed by optoretinography,” *Proc. Natl. Acad. Sci.* **118**(47), e2107444118 (2021).
63. L. Zhang, R. Dong, R. J. Zawadzki, *et al.*, “Volumetric data analysis enabled spatially resolved optoretinogram to measure the functional signals in the living retina,” *J. Biophotonics* **15**(3), e202100252 (2022).
64. S. Tomczewski, P. Węgrzyn, D. Borycki, *et al.*, “Light-adapted flicker optoretinograms captured with a spatio-temporal optical coherence-tomography (STOC-T) system,” *Biomed. Opt. Express* **13**(4), 2186–2201 (2022).
65. S. Gao, Y. Zeng, Y. Li, *et al.*, “Fast and slow light-induced changes in murine outer retina optical coherence tomography: complementary high spatial resolution functional biomarkers,” *PNAS Nexus* **1**(4), pgac208 (2022).
66. I. Erchova, A. R. Tumlinson, J. Fergusson, *et al.*, “Optophysiological characterisation of inner retina responses with high-resolution optical coherence tomography,” *Sci. Rep.* **8**(1), 1813 (2018).
67. C. Pfäffe, H. Spahr, L. Kutzner, *et al.*, “Simultaneous functional imaging of neuronal and photoreceptor layers in living human retina,” *Opt. Lett.* **44**(23), 5671–5674 (2019).